



Winter particulate pollution severity in North China driven by atmospheric teleconnections

Jiandong Li¹, Xin Hao^{2,3}, Hong Liao¹✉, Yuhang Wang⁴, Wenju Cai^{5,6}, Ke Li¹, Xu Yue¹, Yang Yang¹, Haishan Chen⁷, Yuhao Mao¹, Yu Fu^{8,9}, Lei Chen¹ and Jia Zhu¹

Elevated levels of particulate matter in the atmosphere are hazardous to human health and the environment. Severe particulate pollution days, with daily mean PM_{2.5} concentrations exceeding 150 µg m⁻³, occurred frequently in North China, especially during the boreal winters of 2013–2019. Severe particulate pollution generally occurs under conducive weather patterns characterized by a stable atmosphere with weak winds, under which air pollutants emitted at the surface by human activities would accumulate. The occurrence of conducive weather patterns has been attributed to variations in numerous climate factors such as Arctic sea-ice cover, sea surface temperature and atmospheric teleconnections, but the dominant climate drivers remain unclear. Here, we show that the East Atlantic–West Russia teleconnection pattern and the Victoria mode of sea surface temperature anomalies are the top two dominant climate drivers that lead to conducive weather patterns in North China through the zonal and meridional propagations of Rossby waves. Our results suggest that, with the help of seasonal forecast from climate models, indices of these two drivers can be used to predict severe particulate pollution over North China for the coming winter, enabling us to protect human health by air-quality planning.

North China, especially the Beijing–Tianjin–Hebei (BTH) region, frequently experiences severe particulate pollution days (SPPDs, days when the daily mean concentration of particulate matter <2.5 µm (PM_{2.5}) exceeds 150 µg m⁻³) in boreal winter (December, January and February (DJF))^{1,2}, which have essential impacts on visibility³, ecosystems⁴, human health^{5,6} and climate⁷. During January 2013, the observed PM_{2.5} concentrations reached as high as 680 µg m⁻³ in Beijing⁸. Although stringent clean-air regulations have since been implemented in China, and the annual mean PM_{2.5} concentration in China decreased by approximately 33% over 2013–2017⁹, unexpected SPPDs still occurred in Beijing during the COVID-19 lockdown period (January–February 2020)^{10,11}. Therefore, understanding the mechanisms responsible for the occurrence of SPPDs is important for air-quality management planning.

While their underlying cause is attributed to high anthropogenic emissions associated with rapid economic development, SPPDs generally occur under conducive weather patterns (CWPs) favourable to the formation and accumulation of pollutants¹². The atmospheric circulation pattern over North China during haze days was characterized by weakened northerlies and the development of a temperature inversion in the lower troposphere¹³, a weakened East Asian Trough in the mid-troposphere and a northward shift of the East Asian jet in the upper troposphere¹⁴. Similar anomalous atmospheric circulation patterns were also reported in other studies^{1,15,16}. These features of CWPs were obtained from the

composite analysis of haze days, or SPPDs. Nevertheless, CWPs should be further classified to quantify the occurrence frequency of each CWP and to understand how climate drivers help shape different CWPs.

Previous studies suggested that various climate factors are correlated with variations in haze pollution throughout China on interannual to decadal timescales¹⁷. For example, the weakening of the East Asian winter monsoon increased the average concentrations of PM_{2.5} in North China^{18,19}. The reduced autumn Arctic sea-ice cover was reported to result in a more stable atmosphere and hence more haze days in the following winter in eastern China²⁰. Sea surface temperature anomalies (SSTAs) in the Pacific Ocean^{15,21–23}, Atlantic Ocean²¹ and Indian Ocean²⁴ were found to be linked with variations in haze days. Furthermore, teleconnections, such as the East Atlantic–West Russia (EA/WR) pattern²⁵ and the Eurasian pattern²⁶, cause the formation of SPPDs by inducing anomalous circulation conditions. CWPs are also projected to increase under future scenarios of climate warming^{1,27–29}. However, previous studies usually focused on a single climate factor. As such, the climate factors that are predominantly responsible for most SPPDs remain unclear.

Here we show that the EA/WR teleconnection pattern is the dominant climate driver for SPPDs in BTH. We employed PM_{2.5} observations in BTH during DJF of 2013–2019 from the observational network of the Chinese Ministry of Ecology and Environment (Fig. 1a) and identified the CWPs for SPPDs by using a weather

¹Jiangsu Key Laboratory of Atmospheric Environment Monitoring and Pollution Control, Jiangsu Collaborative Innovation Center of Atmospheric Environment and Equipment Technology, School of Environmental Science and Engineering, Nanjing University of Information Science and Technology, Nanjing, China. ²Collaborative Innovation Center on Forecast and Evaluation of Meteorological Disasters/Key Laboratory of Meteorological Disaster, Ministry of Education, Nanjing University of Information Science and Technology, Nanjing, China. ³Nansen-Zhu International Research Centre, Institute of Atmospheric Physics, Chinese Academy of Sciences, Beijing, China. ⁴School of Earth and Atmospheric Sciences, Georgia Institute of Technology, Atlanta, GA, USA. ⁵Key Laboratory of Physical Oceanography–Institute for Advanced Ocean Studies, Ocean University of China and Qingdao National Laboratory for Marine Science and Technology, Qingdao, China. ⁶Centre for Southern Hemisphere Oceans Research (CSHOR), CSIRO Oceans and Atmosphere, Hobart, Tasmania, Australia. ⁷Key Laboratory of Meteorological Disaster, Ministry of Education (KLME)/Joint International Research Laboratory of Climate and Environment Change (ILCEC)/ Collaborative Innovation Center on Forecast and Evaluation of Meteorological Disasters (CIC-FEMD), Nanjing University of Information Science and Technology (NUIST), Nanjing, China. ⁸Climate Change Research Center, Chinese Academy of Sciences, Beijing, China. ⁹Carbon Neutrality Research Center, Institute of Atmospheric Physics, Chinese Academy of Sciences, Beijing, China. ✉e-mail: hongliao@nuist.edu.cn

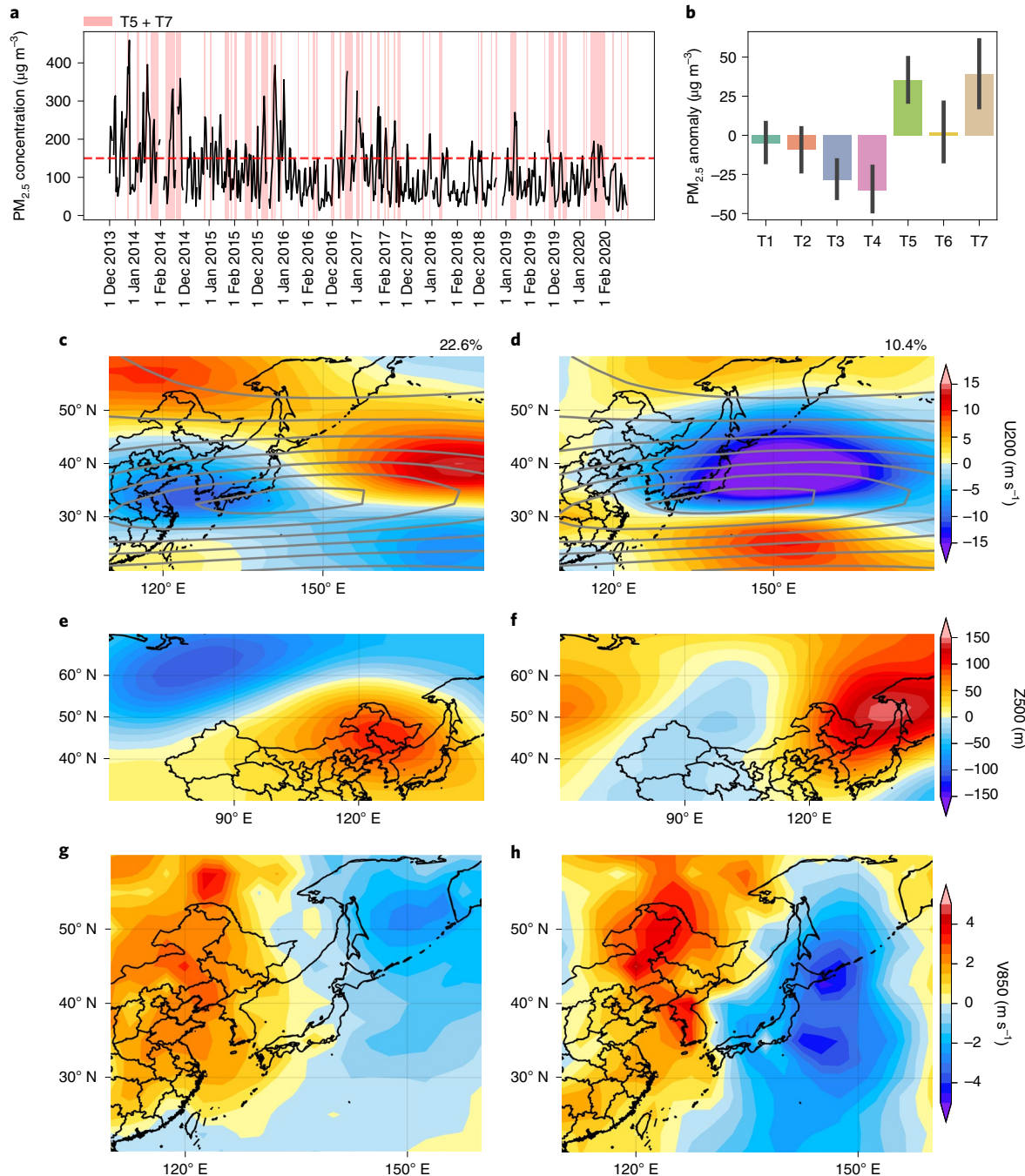


Fig. 1 | Conductive weather patterns favourable for formation of SPPDs. **a**, Time series of the daily average $PM_{2.5}$ over BTH during DJF in 2013–2019 (black line). The red dashed line is the $150 \mu g m^{-3}$ threshold used to define SPPDs. The highlighted pink rectangles represent the occurrences of T5 + T7 weather patterns for the identified CWP. **b**, Mean anomalies of $PM_{2.5}$ relative to the mean of 2013–2019 for each weather type; the error bars are computed on the basis of a normal distribution 95% confidence interval. T5 and T7 are identified as CWPs because of their high positive anomalies. **c–h**, Composites anomalous weather patterns of U200 (**c,d**), Z500 (**e,f**) and V850 (**g,h**) for T5 (**c,e,g**) and T7 (**d,f,h**) over the years 2013–2019. The percentages in **c** and **d** are the frequencies of occurrence for T5 (**c**) and T7 (**d**) during DJF in 2013–2019. The grey contours in **c** and **d** are the western jet streams calculated by DJF means of U200 from 1979 to 2018. T5 displays a northeastward shift of jet stream (**c**) and a weak and shallow East Asian trough (**e**). T7 is associated with a weakened and southward shift of jet stream (**d**), accompanied by a weakened East Asian trough (**f**). Both T5 (**g**) and T7 (**h**) show that positive meridional wind anomalies over BTH reduce the prevailing northwesterly winds to bring less cold and dry air to BTH during winter.

pattern classification approach. We then assigned historical daily DJF circulation patterns during 1979–2019 into CWPs to obtain reconstructed CWPs (R-CWPs). The most dominant climate factor was determined by the highest frequency of R-CWPs caused by that factor.

Typical CWPs for SPPDs and reconstructed historical CWPs
To identify CWPs, we selected the key meteorological variables that drive daily variations in $PM_{2.5}$. Correlations of $PM_{2.5}$ with various meteorological variables, including geopotential height, temperature, winds, relative humidity and sea-level pressure, were

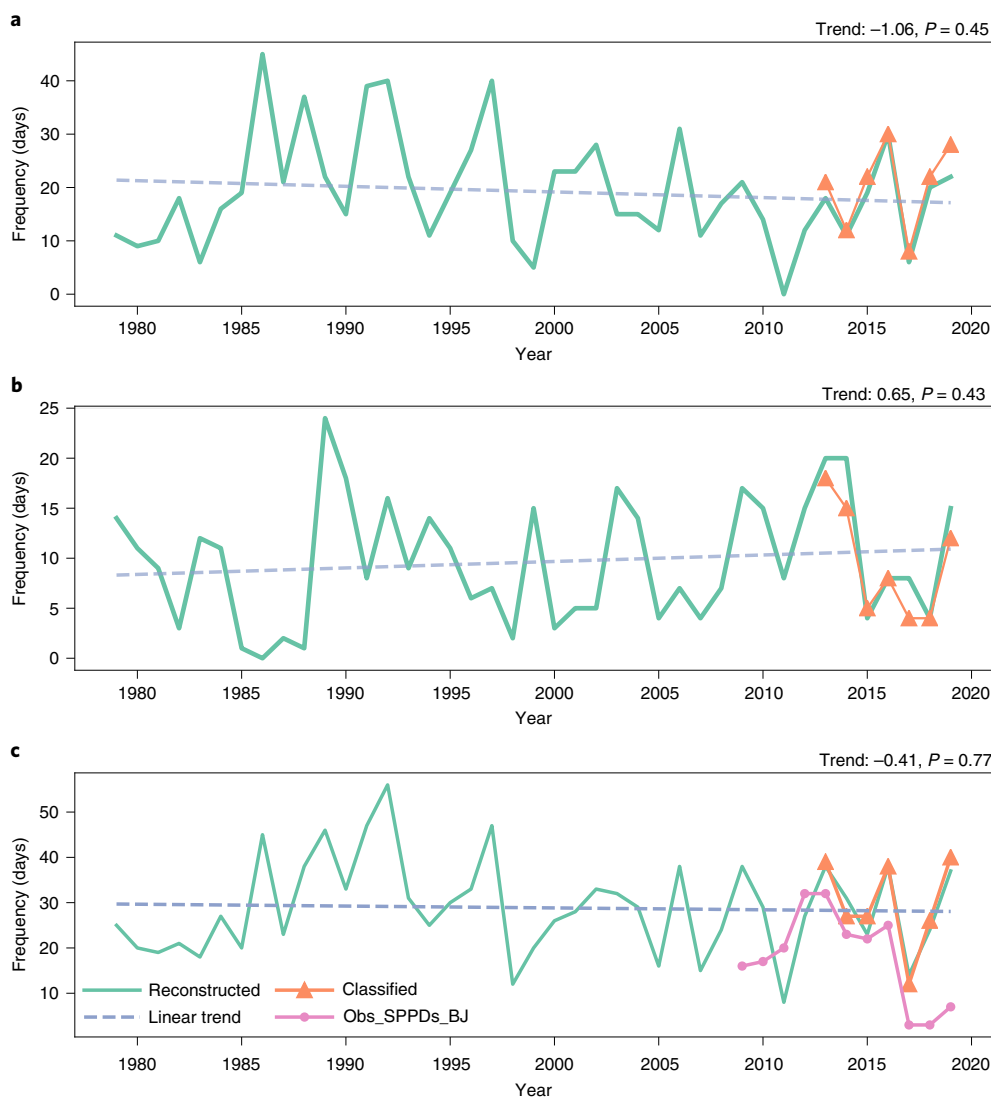


Fig. 2 | Time series of conducive weather patterns and reconstructed conducive weather patterns. a–c, The green lines and orange lines with triangle markers are, respectively, reconstructed (1979–2019) and classified (2013–2019) occurrence frequencies in winter for T5 (**a**), T7 (**b**) and T5 + T7 (**c**). Obs_SPPDs_BJ (**c**) is the observed time series of calculated SPPDs obtained from the US Embassy in Beijing over 2009–2020. ‘Trend’ represents the linear trend calculated by simple linear regression, and P indicates its significance by t test. R-CWPs in 2013–2019 are consistent with classified CWPs. The frequency of T5 + T7 R-CWPs in 2009–2019 can well capture the interannual variations of observed SPPDs in Beijing. The long-term time series of R-CWPs by using multiple reanalysis datasets (see Extended Data Fig. 5) are well matched with each other for the period of 1979–2019. These evaluations indicate the R-CWPs can be used to investigate underlying climate factors inducing SPPDs.

examined during DJF of 2013–2019. High correlations were found with the zonal flow of the upper troposphere at 200 hPa (U200), the geopotential heights at 500 hPa (Z500) and 850 hPa, the meridional flow at 850 hPa (V850), the vertical difference in the temperature anomalies between 850 hPa and 250 hPa, and the relative humidity at 1,000 hPa (Extended Data Fig. 1). Among these variables, U200, Z500 and V850 were ultimately selected considering that climate factors influence CWPs by changing large-scale circulations. These three parameters have also been reported to be important for the formation of SPPDs^{1,14,28}. Assuming that the daily concentration of PM_{2.5} averaged over BTH (x) is related to the daily meteorological variable (y) at a grid cell following $y = ax + b$ (where y is one of U200, Z500 and V850), maps of the regression coefficient (a) were utilized to quantify the meteorological changes in response to PM_{2.5} fluctuations (Extended Data Fig. 2). Then, guided by the highest positive and negative regression coefficients, the meteorological

parameters in the black rectangles in Extended Data Fig. 2a–c were used to classify the CWPs.

By using U200, Z500 and V850 as identified, we classified the daily weather conditions during DJF of 2013–2019 (632 days) into 7 types (Methods, hereafter referred to as T1 through T7, shown in Extended Data Fig. 3). T1 through T7 accounted for 15.2%, 13.0%, 20.1%, 11.6%, 22.6%, 7.1% and 10.4% of the weather conditions among all 632 days. Considering the mean PM_{2.5} concentration, the mean PM_{2.5} anomalies, the number of observed SPPDs and the percentage of SPPDs among that type of wintertime days, the T5 (150.1 $\mu\text{g m}^{-3}$, +35.2 $\mu\text{g m}^{-3}$, 57 days and 43.5%) and T7 (154.2 $\mu\text{g m}^{-3}$, +39.3 $\mu\text{g m}^{-3}$, 29 days and 45.3%) were CWPs that induced the most occurrences of SPPDs, while the T1 (109.5 $\mu\text{g m}^{-3}$, -5.3 $\mu\text{g m}^{-3}$, 24 days and 26.7%), T2 (105.9 $\mu\text{g m}^{-3}$, -9.0 $\mu\text{g m}^{-3}$, 16 days and 22.2%) and T6 (116.9 $\mu\text{g m}^{-3}$, +2.0 $\mu\text{g m}^{-3}$, 10 days and 22.7%) patterns resulted in moderate pollution and the T3

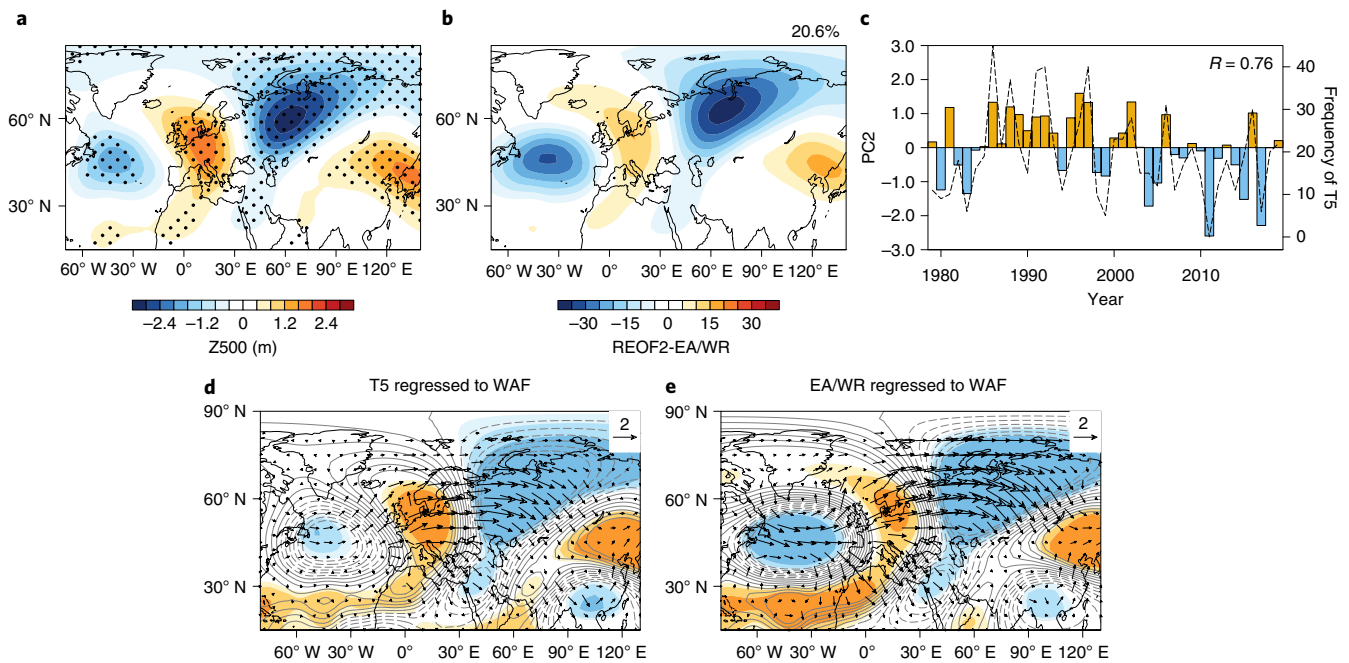


Fig. 3 | Possible mechanism for T5. **a**, Linear regression of the 500 hPa geopotential height (m) with respect to the detrended time series of T5 during DJF for the period 1979–2019. Stippled regions indicate that the regression coefficients are statistically significant at the 95% confidence level based on the Student's *t* test. **b,c**, Spatial pattern of the REOF2 of the 500 hPa geopotential height in winter (**b**) and the associated PC2 (histogram) and frequency of T5 (black dotted line) (**c**). The percentage in **b** is the variance (%) explained by the REOF2. **d,e**, The 200 hPa wave activity flux (WAF) (vector, only values passing the 95% significance level are shown; $10^{-3} \text{ m}^2 \text{ s}^{-2}$ in **d** and $10^{-2} \text{ m}^2 \text{ s}^{-2}$ in **e**) and stream function (contour line; $10^4 \text{ m}^2 \text{ s}^{-1}$ in **d** and $10^5 \text{ m}^2 \text{ s}^{-1}$ in **e**) regressed on the detrended time series of T5 (**d**) and PC2 (**e**). Shaded areas denote significant values of regression coefficient of stream function at 90% (light), 95% (middle) and 99% (dark) confidence levels.

($86.0 \mu\text{g m}^{-3}$, $-28.9 \mu\text{g m}^{-3}$, 14 days and 11.4%) and T4 ($79.6 \mu\text{g m}^{-3}$, $-35.3 \mu\text{g m}^{-3}$, 7 days and 9.7%) patterns corresponded to relatively clean patterns (Fig. 1b and Extended Data Fig. 4). During 2013–2019, there were 157 wintertime SPPDs, of which 86 days (54.8%) occurred under T5 and T7 weather patterns (Fig. 1a). Note that anthropogenic emissions constituted another important factor for the occurrence of SPPDs. For example, SPPDs did not occur following the Chinese Spring Festival due to relatively low emission levels even though the weather patterns were CWP.

Multidecadal data are needed to detect the dominant climate factor leading to CWP since climate represents the long-term average of weather. On the basis of the CWP (T5 and T7) found in the preceding (Fig. 1c–h), the long-term changes in CWP were reconstructed by assigning the historical daily DJF weather conditions during 1979–2019 into T5 and T7 by using the smallest Euclidean distance (Methods). The frequencies of the R-CWP over 1979–2019 show no significant trends but large interannual variations for T5, T7 and T5+T7 (Fig. 2), which are associated with the variations in climate factors as discussed subsequently. We evaluated the R-CWP in several ways. For 2013–2019, the R-CWP agree with the CWP classified using U200, Z500 and V850 (Fig. 2), with correlation coefficients of 0.97, 0.96 and 0.96 for T5, T7 and T5+T7, respectively. The long-term record of observed $\text{PM}_{2.5}$ from the US Embassy in Beijing over 2009–2019 demonstrates that the interannual variation of observed SPPDs matches that of the T5+T7 R-CWP. The low frequencies of observed SPPDs at the US Embassy in Beijing over 2017–2019 indicate the result of the Clean Air Action. The variations in CWP reconstructed using the National Center for Environmental Prediction (NCEP) reanalysis over 1979–2019 resemble those of R-CWP reconstructed by the fifth-generation reanalysis from the European Centre for Medium-Range Weather Forecasts (ERA5), with high correlation

coefficients of 0.93–0.99 (Extended Data Fig. 5). Moreover, the pattern correlations between composite anomalies of the R-CWP during 1979–2019 and those of CWP during 2013–2019 are in the range of 0.88 to 0.99 (Extended Data Fig. 6). Considering these evaluations, we leveraged the T5 and T7 R-CWP in 1979–2019 to identify the dominant climate factors that cause SPPDs.

Dominant climate drivers of SPPDs

We first performed correlation analyses to explore the potential linkage between climate factors and R-CWP. Extended Data Figs. 7–9 show heat maps of the correlation coefficients between T5/T7 and 85 atmospheric indices (Supplementary Table 1) and 26 SST indices (Supplementary Table 2), respectively. We found that T5 is highly correlated with atmospheric teleconnection indices, such as the East Atlantic pattern, the EA/WR pattern and the Asian Zonal Circulation Index (Extended Data Fig. 7). By contrast, T7 is correlated mainly with the SST of the Pacific Ocean, for example, the Oyashio Current SST Index, the Kuroshio Current SST Index, the West Wind Drift Current SST Index and the NINO A SSTA Index (Extended Data Fig. 9). Hence, the dominant climate factors linked to SPPDs in BTH are examined on the basis of these two aspects. Other climate factors, including the Arctic sea ice, atmospheric teleconnections and SST over the Indian and Atlantic oceans, are excluded as described in detail in Supplementary Text 1.

Boreal winter teleconnections, such as the Pacific/North American pattern, the West Pacific pattern and the East Atlantic pattern, can be detected from the geopotential height field at 500 hPa^{30,31}. Hence, we used the annual DJF mean 500 hPa geopotential height to regress the T5 R-CWP over the Eurasian continent from 1979 to 2019 (for each grid in the studied domain, the regression coefficient is calculated by a simple linear regression, $y = ax + b$, where T5 is x and the DJF mean 500 hPa geopotential height is y ;

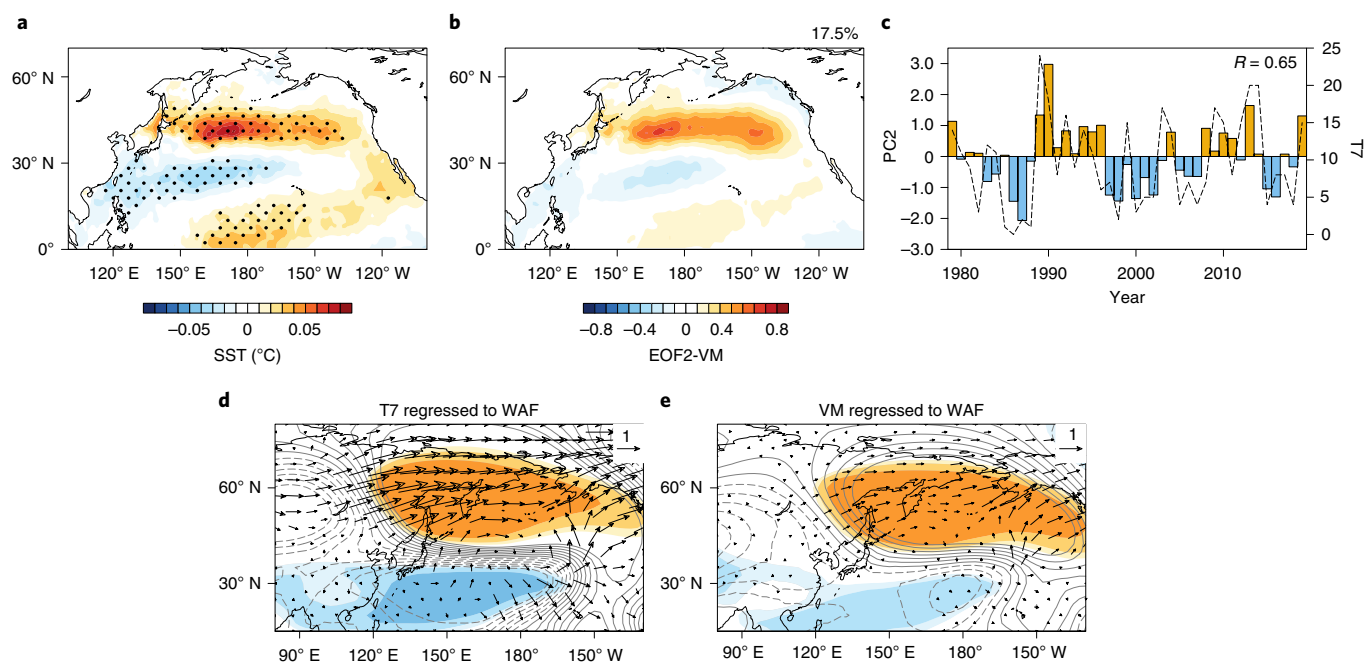


Fig. 4 | Possible mechanism for T7. **a**, SST regressed on the detrended time series of T7. Stippled regions indicate that the regression coefficients are statistically significant at the 95% confidence level based on the Student's *t* test. **b**, EOF2 of the SSTAs in the North Pacific polewards of 20° N. The percentage in **b** is the variance (%) explained by the EOF2. **c**, PC2 of the VM (histogram) and frequency of T7 (black dotted line) for the period 1979–2019. **d, e**, The 200 hPa wave activity flux (vector; $10^{-2} \text{ m}^2 \text{ s}^{-2}$ in **d** and $10^{-2} \text{ m}^2 \text{ s}^{-2}$ in **e**) and stream function (contour line; $10^4 \text{ m}^2 \text{ s}^{-1}$ in **d** and $10^5 \text{ m}^2 \text{ s}^{-1}$ in **e**) regressed on the detrended seasonal time series of T7 (**d**) and PC2 (**e**) in DJF for the period 1979–2019. Shaded areas denote significant values of regression coefficient of stream function at 90% (light), 95% (middle) and 99% (dark) confidence levels.

thus, the regression coefficient, a , indicates the Z500 anomaly in response to changes in T5). Figure 3a shows the spatial distribution of the regression coefficient, revealing a planetary-scale stationary wave pattern extending to the North Atlantic Ocean at approximately 45° N, western Europe, central Russia and mid-latitude East Asia with alternating positive/negative anomalies. This pattern is similar to the EA/WR pattern, whose impact extends from the North Atlantic to the whole Eurasian mainland^{32,33}. On the basis of these findings, we examined the leading modes of large-scale teleconnections from the DJF mean 500 hPa geopotential height field. The spatial distribution of the second rotated empirical orthogonal function (REOF2) mode eigenvector (Fig. 3b), which represents the EA/WR pattern, displays nearly the same structure as the regression map of the 500 hPa geopotential height on T5. A close correlation is found between T5 and the time series of the corresponding second principal component (PC2, Fig. 3c), with a statistically significant correlation coefficient of 0.76.

The EA/WR pattern is essentially tied to large-scale stationary waves, which are forced by vorticity transients in the mid-latitude Atlantic or by a diabatic heat source over the subtropical Atlantic near the Caribbean Sea³³. Horizontal wave activity fluxes (Methods) at 200 hPa associated with the EA/WR pattern show that a source of the wave train is located over the mid-latitude Atlantic at approximately 40° N; the wave train propagates eastwards and branches at 15° W (Fig. 3e), whereupon one branch extends to East Asia via western Europe and western Russia, while the other branch propagates southeastwards to the Middle East via West Africa (Fig. 3e). Note that the horizontal wave activity fluxes associated with T5 display a clear wave-train pattern extending from the mid-latitude North Atlantic to East Asia through western Europe and western Russia, which closely matches the North Atlantic–Eurasian route of Rossby wave propagation associated with the EA/WR pattern (Fig. 3d). As for T5 (Fig. 1c,e,g), the northeastward-shifted jet

stream acts as a wave guide for Rossby waves, motivating a weak and shallow East Asian Trough to obstruct the southward outbreak of cold air. This suggests that the EA/WR pattern is responsible for T5 CWP over BTH. Considering that T5 is the most frequent weather pattern (accounting for 22.6% of wintertime days in 2013–2019, 21.6% of wintertime days in 1979–2019 and 36.3% of the observed SPPDs in 2013–2019), the EA/WR pattern is identified as the dominant climate factor that leads to SPPDs in BTH.

The reconstructed time series of T7 display a statistically significant relationship with the SSTAs in the North Pacific Ocean. As shown in Fig. 4a, the linear coefficients of SST regressed on the T7 R-CWPs time series exhibit a northeast–southwest-oriented dipole pattern in the North Pacific polewards of 20° N; this pattern is characterized by a band of positive anomalies extending from the western coast of North America across the Pacific to the western Bering Sea and a band of negative anomalies extending from the coast of Asia to the central North Pacific. Weak positive correlations were also found in the tropical central North Pacific (Fig. 4a). When these features are considered together, the regression map seems to display a Victoria mode (VM) SSTA³⁴. Figure 4b shows the VM, which is defined as the EOF2 of the SSTAs in the North Pacific polewards of 20° N^{34,35}. The spatial distribution of the VM resembles the SSTA pattern associated with T7, and the correlation coefficient between the two time series is 0.65 (Fig. 4c).

Previous studies indicated that the VM pattern imparted from the North Pacific Oscillation can induce overlying atmospheric anomalies, leading to an anomalous wintertime zonal wind stress over the North Pacific^{34,36}. Figure 4e shows the wave activity flux and stream function regressed on the normalized VM index at 200 hPa, illustrating that a Rossby wave train originates from the western North Pacific probably induced by heat flux anomalies associated with western-boundary currents and propagates northwards to northern East Asia and then eastwards to the high-latitude

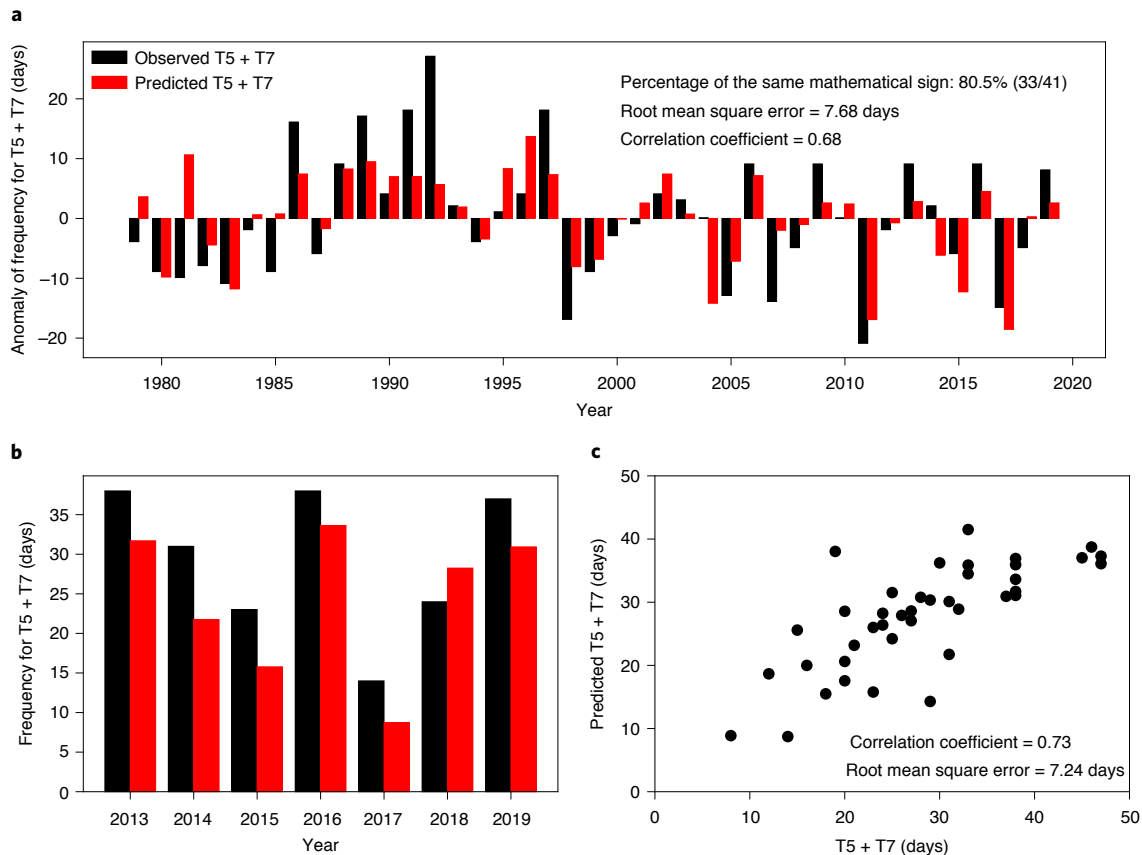


Fig. 5 | Evaluation of the ability to predict the frequency of CWP by EA/WR and VM. **a**, Verification for the cross-validation test during 1979–2019. Predicted CWP of each target year were calculated by an empirical prediction model established with the remaining 40-year data. Anomalies with respect to 1979–2019 means for predicted and observed CWP are shown. **b**, Performance of independent hindcasts. The period of 1979–2012 was used for training empirical prediction model. CWP in each year of 2013–2019 were predicted (red histogram) and compared with the observed CWP (black histogram) of 2013–2019. **c**, Scatter plot of predicted frequency for T5 + T7 CWP by empirical prediction model train spanning historical period of 1979–2019 and observed frequency for T5 + T7 CWP in Fig. 2c.

North Pacific. This corresponding Rossby wave train provides a connection between the VM and East Asian regional circulation. The Rossby wave associated with the T7 R-CWP displays a similar propagation pattern (Fig. 4d) to East Asia along the weakened and southward-shifted jet stream, leading to a weakened East Asian Trough and stable weather conditions (Fig. 1d,f). Consequently, northwesterly winds are impaired, and thus, they transport less cold and dry air to BTH during winter (Fig. 1h). The overall similarities between the T7 R-CWP and VM imply a dynamic link between the VM and SPPDs in BTH. Note that the meridional dipolar anomaly over East Asia can also be partly influenced by internal variability of Western Pacific teleconnection³⁷. Compared with T5, T7 has a lower frequency of occurrence, accounting for 10.4% of wintertime days in 2013–2019, 10.6% of wintertime days in 1979–2019 and 18.5% of the observed SPPDs in 2013–2019.

Prediction ability of the dominant climate drivers

Since there is no linearity relationship between time series of the EA/WR and VM ($R=0.12$), they can be used to predict the frequency of CWP in BTH. A statistical scheme is established using the multi-linear regression method, $y=ax_1+bx_2+c$, in which two predictors (x_1 and x_2) denote the EA/WR and VM, while y denotes the predicted (observed) frequency of CWP for T5 + T7, with a/b and c being regression coefficients and intercept. Both cross validation and independent hindcast were carried out to verify the capability of predicting CWP. For cross validation, a one-year-out

cross-validation approach was used, with any individual year out of 1979–2019 being the target year and the multi-linear regression established for the remaining 40 years. As for independent hindcasts, the period of 1979–2012 was used for training and another period of 2013–2019 was used for the evaluation of prediction. Figure 5a shows the 1979–2019 cross-validation test. The correlation coefficient, root mean square error and percentage of the same mathematical sign in Fig. 5a are 0.68, 7.68 days and 80.5% (33/41), respectively, indicating a proper stability of our prediction model. In Fig. 5b, the predicted CWP by independent hindcast can successfully reproduce the interannual variability of observed CWP in 2013–2019. The overall period 1979–2019 predictions have a significant correlation with observations, with correlation coefficient and root mean square error being 0.73 and 7.24 days (Fig. 5c), respectively. Therefore, we conclude that, with the help of seasonal forecast from climate models (Supplementary Text 2), the EA/WR and VM can be used to predict the future wintertime frequency of CWP in BTH.

In summary, in this study, we identified the dominant climate factors that cause wintertime SPPDs in BTH. The EA/WR teleconnection pattern was found to be the dominant climate factor (inducing 36.3% of the observed SPPDs over 2013–2019) that results in CWP for SPPDs in North China through the propagation of large-scale stationary waves originating from the mid- to high latitudes of the North Atlantic to East Asia via western Europe and western Russia. The VM SSTAs in the North Pacific Ocean were

found to be the second predominant climate factor (inducing 18.5% of the observed SPPDs over 2013–2019) leading to SPPDs in North China by a wave train extending from the western North Pacific to the high-latitude North Pacific. The indices of the EA/WR and VM (Figs. 3c and 4c) can be used to predict wintertime SPPDs over BTH, offering guidance for emission reduction strategy.

Online content

Any methods, additional references, Nature Research reporting summaries, source data, extended data, supplementary information, acknowledgements, peer review information; details of author contributions and competing interests; and statements of data and code availability are available at <https://doi.org/10.1038/s41561-022-00933-2>.

Received: 27 September 2020; Accepted: 17 March 2022;

Published online: 21 April 2022

References

- Cai, W., Li, K., Liao, H., Wang, H. & Wu, L. Weather conditions conducive to Beijing severe haze more frequent under climate change. *Nat. Clim. Change* **7**, 257–262 (2017).
- Li, J., Liao, H., Hu, J. & Li, N. Severe particulate pollution days in China during 2013–2018 and the associated typical weather patterns in Beijing–Tianjin–Hebei and the Yangtze River delta regions. *Environ. Pollut.* **248**, 74–81 (2019).
- Yang, Y., Liao, H. & Lou, S. Increase in winter haze over eastern China in recent decades: roles of variations in meteorological parameters and anthropogenic emissions. *J. Geophys. Res. Atmos.* **121**, 13050–13065 (2016).
- Yue, X. et al. Ozone and haze pollution weakens net primary productivity in China. *Atmos. Chem. Phys.* **17**, 6073–6089 (2017).
- Hu, J. et al. Premature mortality attributable to particulate matter in China: source contributions and responses to reductions. *Environ. Sci. Technol.* **51**, 9950–9959 (2017).
- Hao, X. et al. Long-term health impact of PM_{2.5} under whole-year COVID-19 lockdown in China. *Environ. Pollut.* **290**, 118118 (2021).
- Li, Z. et al. Aerosol and monsoon climate interactions over Asia. *Rev. Geophys.* **54**, 866–929 (2016).
- Wang, Y. et al. Mechanism for the formation of the January 2013 heavy haze pollution episode over central and eastern China. *Sci. China Earth Sci.* **57**, 14–25 (2014).
- Zhang, Q. et al. Drivers of improved PM_{2.5} air quality in China from 2013 to 2017. *Proc. Natl Acad. Sci. USA* **116**, 24463–24469 (2019).
- Huang, X. et al. Enhanced secondary pollution offset reduction of primary emissions during COVID-19 lockdown in China. *Natl Sci. Rev.* **8**, nwaal37 (2020).
- Wang, P., Chen, K., Zhu, S., Wang, P. & Zhang, H. Severe air pollution events not avoided by reduced anthropogenic activities during COVID-19 outbreak. *Resour. Conserv. Recycl.* **158**, 104814 (2020).
- Zhao, X. J. et al. Analysis of a winter regional haze event and its formation mechanism in the North China Plain. *Atmos. Chem. Phys.* **13**, 5685–5696 (2013).
- Liu, C. et al. A severe fog-haze episode in Beijing–Tianjin–Hebei region: characteristics, sources and impacts of boundary layer structure. *Atmos. Pollut. Res.* **10**, 1190–1202 (2019).
- Chen, H. & Wang, H. Haze days in North China and the associated atmospheric circulations based on daily visibility data from 1960 to 2012. *J. Geophys. Res. Atmos.* **120**, 5895–5909 (2015).
- Pei, L., Yan, Z., Sun, Z., Miao, S. & Yao, Y. Increasing persistent haze in Beijing: potential impacts of weakening East Asian winter monsoons associated with northwestern Pacific sea surface temperature trends. *Atmos. Chem. Phys.* **18**, 3173–3183 (2018).
- Wu, P., Ding, Y. & Liu, Y. Atmospheric circulation and dynamic mechanism for persistent haze events in the Beijing–Tianjin–Hebei region. *Adv. Atmos. Sci.* **34**, 429–440 (2017).
- An, Z. et al. Severe haze in northern China: a synergy of anthropogenic emissions and atmospheric processes. *Proc. Natl Acad. Sci. USA* **116**, 8657–8666 (2019).
- Zhao, S., Feng, T., Tie, X., Li, G. & Cao, J. Air pollution zone migrates south driven by East Asian winter monsoon and climate change. *Geophys. Res. Lett.* **48**, e2021GL092672 (2021).
- Wu, G. et al. Advances in studying interactions between aerosols and monsoon in China. *Sci. China Earth Sci.* **59**, 1–16 (2016).
- Wang, H., Chen, H. & Liu, J. Arctic sea ice decline intensified haze pollution in eastern China. *Atmos. Ocean Sci. Lett.* **8**, 1–9 (2015).
- Wang, J. et al. Two pathways of how remote SST anomalies drive the interannual variability of autumnal haze days in the Beijing–Tianjin–Hebei region, China. *Atmos. Chem. Phys.* **19**, 1521–1535 (2019).
- Yin, Z. & Wang, H. The relationship between the subtropical western Pacific SST and haze over north-central North China Plain. *Int. J. Climatol.* **36**, 3479–3491 (2016).
- Chen, S., Guo, J., Song, L., Cohen, J. B. & Wang, Y. Temporal disparity of the atmospheric systems contributing to interannual variation of wintertime haze pollution in the North China Plain. *Int. J. Climatol.* **40**, 128–144 (2020).
- Shen, L., Jacob, D. J., Mickley, L. J., Wang, Y. & Zhang, Q. Insignificant effect of climate change on winter haze pollution in Beijing. *Atmos. Chem. Phys.* **18**, 17489–17496 (2018).
- Yin, Z. & Wang, H. Role of atmospheric circulations in haze pollution in December 2016. *Atmos. Chem. Phys.* **17**, 11673–11681 (2017).
- Zou, Y., Wang, Y., Xie, Z., Wang, H. & Rasch, P. J. Atmospheric teleconnection processes linking winter air stagnation and haze extremes in China with regional Arctic sea ice decline. *Atmos. Chem. Phys.* **20**, 4999–5017 (2020).
- Zou, Y., Wang, Y., Zhang, Y. & Koo, J. H. Arctic sea ice, Eurasia snow, and extreme winter haze in China. *Sci. Adv.* **3**, e1602751 (2017).
- Pei, L. & Yan, Z. Diminishing clear winter skies in Beijing towards a possible future. *Environ. Res. Lett.* **13**, 124029 (2018).
- Chen, H., Wang, H., Sun, J., Xu, Y. & Yin, Z. Anthropogenic fine particulate matter pollution will be exacerbated in eastern China due to 21st century GHG warming. *Atmos. Chem. Phys.* **19**, 233–243 (2019).
- Wallace, J. M. & Gutzler, D. S. Teleconnections in the geopotential height field during the Northern Hemisphere winter. *Mon. Weather Rev.* **109**, 784–812 (1981).
- Horel, J. D. & Wallace, J. M. Planetary-scale atmospheric phenomena associated with the Southern Oscillation. *Mon. Weather Rev.* **109**, 813–829 (1981).
- Krichak, S. O., Breitgand, J. S., Gualdi, S. & Feldstein, S. B. Teleconnection–extreme precipitation relationships over the Mediterranean region. *Theor. Appl. Climatol.* **117**, 679–692 (2013).
- Lim, Y.-K. The East Atlantic/West Russia (EA/WR) teleconnection in the North Atlantic: climate impact and relation to Rossby wave propagation. *Clim. Dyn.* **44**, 3211–3222 (2014).
- Ding, R., Li, J., Tseng, Y.-h., Sun, C. & Guo, Y. The Victoria mode in the North Pacific linking extratropical sea level pressure variations to ENSO. *J. Geophys. Res. Atmos.* **120**, 27–45 (2015).
- Bond, N. A., Overland, J. E., Spillane, M. & Stabeno, P. Recent shifts in the state of the North Pacific. *Geophys. Res. Lett.* **30**, 2183 (2003).
- Ding, R., Li, J., Tseng, Y.-h., Sun, C. & Zheng, F. Linking a sea level pressure anomaly dipole over North America to the central Pacific El Niño. *Clim. Dyn.* **49**, 1321–1339 (2017).
- Tanaka, S., Nishii, K. & Nakamura, H. Vertical structure and energetics of the western Pacific teleconnection pattern. *J. Clim.* **29**, 6597–6616 (2016).

Publisher's note Springer Nature remains neutral with regard to jurisdictional claims in published maps and institutional affiliations.

© The Author(s), under exclusive licence to Springer Nature Limited 2022

Methods

Observation data. The PM_{2.5} data from December 2013 to February 2020 used in this study are obtained from the Chinese Ministry of Ecology and Environment. A longer record of PM_{2.5} dataset over 2009–2020 from the US Embassy in Beijing is also used. This dataset has been widely used in previous studies and is reported to well represent PM_{2.5} variation in BTH^{1,29,38–40}. The daily average PM_{2.5} is processed and quality controlled following a previous study². The cities with continuous PM_{2.5} observations since 2013 are displayed in Extended Data Fig. 1a. Daily meteorology fields, including geopotential heights and winds at different pressure levels and mean sea-level pressure, are from the fifth-generation reanalysis from ERA5 with a resolution of 2.5° × 2.5° downloaded from the Copernicus Climate Change Service (2017)⁴¹. Daily outputs from NCEP/NCAR Reanalysis 1 (NCEP1)⁴² and NCEP-DOE Reanalysis 2 (NCEP2)⁴³, including U200, Z500 and V850, were also utilized to construct R-CWPs for comparison with ERA5 R-CWPs.

The observed SSTs are from the Hadley Centre⁴⁴. The anomaly of a parameter on a specific day is calculated relative to the daily climatology spanning 40 years (1979–2018). The EA/WR pattern is defined as the second leading rotated empirical orthogonal function mode of the 500 hPa geopotential height in the region 15°–85°N, 70°W–140°E^{30,45}, and its climate impact extends from eastern North America to Eurasia through wave-train propagation. The VM is defined as the second leading mode of the SST in the North Pacific Ocean (20°–61°N, 100°E–80°W).

Classification of weather patterns during SPPDs. We identify the wintertime typical weather patterns during 2013–2019 by using obliquely rotated principal component analysis in T mode (T-PCA), which is commonly used to classify circulation patterns⁴⁶. This method has also been employed to investigate the circulation patterns that are conducive to particulate pollution in North China^{3,47,48} and the Yangtze River delta⁴⁹. In this study, we use the T-PCA method in the Cost733class software package (<http://cost733.met.no>) to identify typical circulation patterns during DJF in BTH from 2013 to 2019. More details of the T-PCA procedure in Cost733class can be found in the literature^{2,50}. In addition to the three key meteorological parameters of U200, Z500 and V850, we test other associated variables reported by previous studies. As shown in Extended Data Fig. 2, the regions with maximum variability of the near-surface relative humidity (RH1000, Extended Data Fig. 2d) are too regional compared with U200, Z500 and V850, leading to little influence on the classification results. The regression coefficients of the temperature inversion (Extended Data Fig. 2e) display nearly the same pattern as those of Z500 (Extended Data Fig. 2b).

The classification performance is evaluated by the explained variation and pseudo *F* values (Extended Data Fig. 4a). Seven weather patterns are classified, among which two conducive weather pattern types are identified. Although six classifications result in better performance from a meteorological perspective, seven types can better distinguish the CWPs (Extended Data Fig. 4b–e). After selecting the appropriate classification, historical daily DJF weather samples from 1979 to 2019 are assigned to the corresponding CWPs with the smallest Euclidean distance, which is also performed in the Cost733class software⁵¹.

Wave activity fluxes. The dynamic mechanism by which a climate factor (or pattern) leads to CWPs for the formation of SPPDs is usually a teleconnection, which can be measured by wave activities⁵². In this study, the horizontal wave-train flux⁵³ is calculated by using meteorological variables (for example, geopotential height, air density and pressure level) to display the stream function (wave energy pattern) and intensity and direction of wave propagation. On the basis of the horizontal wave-train flux, we can diagnose the source and propagation direction of stationary waves that lead to CWPs for the formation of SPPDs. This approach has been widely used to examine the relationship between climate factors and circulation patterns for haze pollution in China^{20,21,25}.

Data availability

The analytic data that support the major results are accessible at figshare (<https://figshare.com/s/be3b2c64e0757e805bf7>). The surface PM_{2.5} observations from the Chinese Ministry of Ecology and Environment can be obtained from <http://106.37.208.233:20035/> and <https://quotsoft.net/air/>. The surface PM_{2.5} observations for the US Embassy in Beijing are downloaded from [https://www.airnow.gov/international/us-embassies-and-consulates/#China\\$Beijing](https://www.airnow.gov/international/us-embassies-and-consulates/#China$Beijing). The ERA5 reanalysis data are available from <https://cds.climate.copernicus.eu/cdsapp#!/search>. The NCEP1 reanalysis data are available from <https://psl.noaa.gov/data/gridded/data.ncep.reanalysis.html>. The NCEP2 reanalysis data are available from <https://psl.noaa.gov/data/gridded/data.ncep.reanalysis2.html>. The observed sea surface temperatures from the Hadley Centre are downloaded from <https://www.metoffice.gov.uk/hadobs/hadisst/data/download.html>. Source data are provided with this paper.

Code availability

The Cost733class software is open source (<http://cost733.met.no/>).

References

- Shen, G. et al. Impacts of air pollutants from rural Chinese households under the rapid residential energy transition. *Nat. Commun.* **10**, 3405 (2019).
- Dang, R. & Liao, H. Severe winter haze days in the Beijing–Tianjin–Hebei region from 1985 to 2017 and the roles of anthropogenic emissions and meteorology. *Atmos. Chem. Phys.* **19**, 10801–10816 (2019).
- Zhang, Y., Yin, Z. & Wang, H. Roles of climate variability on the rapid increases of early winter haze pollution in North China after 2010. *Atmos. Chem. Phys.* **20**, 12211–12221 (2020).
- Hersbach, H. et al. The ERA5 global reanalysis. *Q. J. R. Meteorol. Soc.* **146**, 1999–2049 (2020).
- Kalnay, E. et al. The NCEP/NCAR 40-year reanalysis project. *Bull. Am. Meteorol. Soc.* **77**, 437–472 (1996).
- Kanamitsu, M. et al. NCEP-DOE AMIP-II Reanalysis (R-2). *Bull. Am. Meteorol. Soc.* **83**, 1631–1644 (2002).
- Rayner, N. A. Global analyses of sea surface temperature, sea ice, and night marine air temperature since the late nineteenth century. *J. Geophys. Res.* **108**, 4407 (2003).
- Barnston, A. G. & Livezey, R. E. Classification, seasonality and persistence of low-frequency atmospheric circulation patterns. *Mon. Weather Rev.* **115**, 1083–1126 (1987).
- Huth, R. et al. Classifications of atmospheric circulation patterns: recent advances and applications. *Ann. N. Y. Acad. Sci.* **1146**, 105–152 (2008).
- Zhang, J. P. et al. The impact of circulation patterns on regional transport pathways and air quality over Beijing and its surroundings. *Atmos. Chem. Phys.* **12**, 5031–5053 (2012).
- Wang, X. & Zhang, R. Effects of atmospheric circulations on the interannual variation in PM_{2.5} concentrations over the Beijing–Tianjin–Hebei region in 2013–2018. *Atmos. Chem. Phys.* **20**, 7667–7682 (2020).
- Xu, J. et al. The meteorological modulation on PM_{2.5} interannual oscillation during 2013 to 2015 in Shanghai, China. *Sci. Total Environ.* **572**, 1138–1149 (2016).
- Philipp, A. et al. Cost733cat—a database of weather and circulation type classifications. *Phys. Chem. Earth Part A/B/C* **35**, 360–373 (2010).
- Murawski, A., Bürger, G., Vorogushyn, S. & Merz, B. Can local climate variability be explained by weather patterns? A multi-station evaluation for the Rhine basin. *Hydrol. Earth Syst. Sci.* **20**, 4283–4306 (2016).
- Boers, N. et al. Complex networks reveal global pattern of extreme-rainfall teleconnections. *Nature* **566**, 373–377 (2019).
- Plumb, R. A. On the three-dimensional propagation of stationary waves. *J. Atmos. Sci.* **42**, 217–229 (1985).

Acknowledgements

H.L. acknowledges the National Natural Science Foundation of China (grant nos. 42021004 and 91744311) and the Major Research Plan of the National Social Science Foundation (grant no. 18ZDA052). X.H. is supported by the National Natural Science Foundation of China (grant no. 42088101) and the Guangdong Major Project of Basic and Applied Basic Research (grant no. 2020B0301030004).

Author contributions

J.L., X.H. and H.L. conceived the study. J.L. and X.H. performed the data analysis. Y.W. and W.C. contributed to interpreting the scientific questions. J.L., X.H. and H.L. wrote the draft of the manuscript. All authors contributed to discussing and improving the manuscript.

Competing interests

The authors declare no competing interests.

Additional information

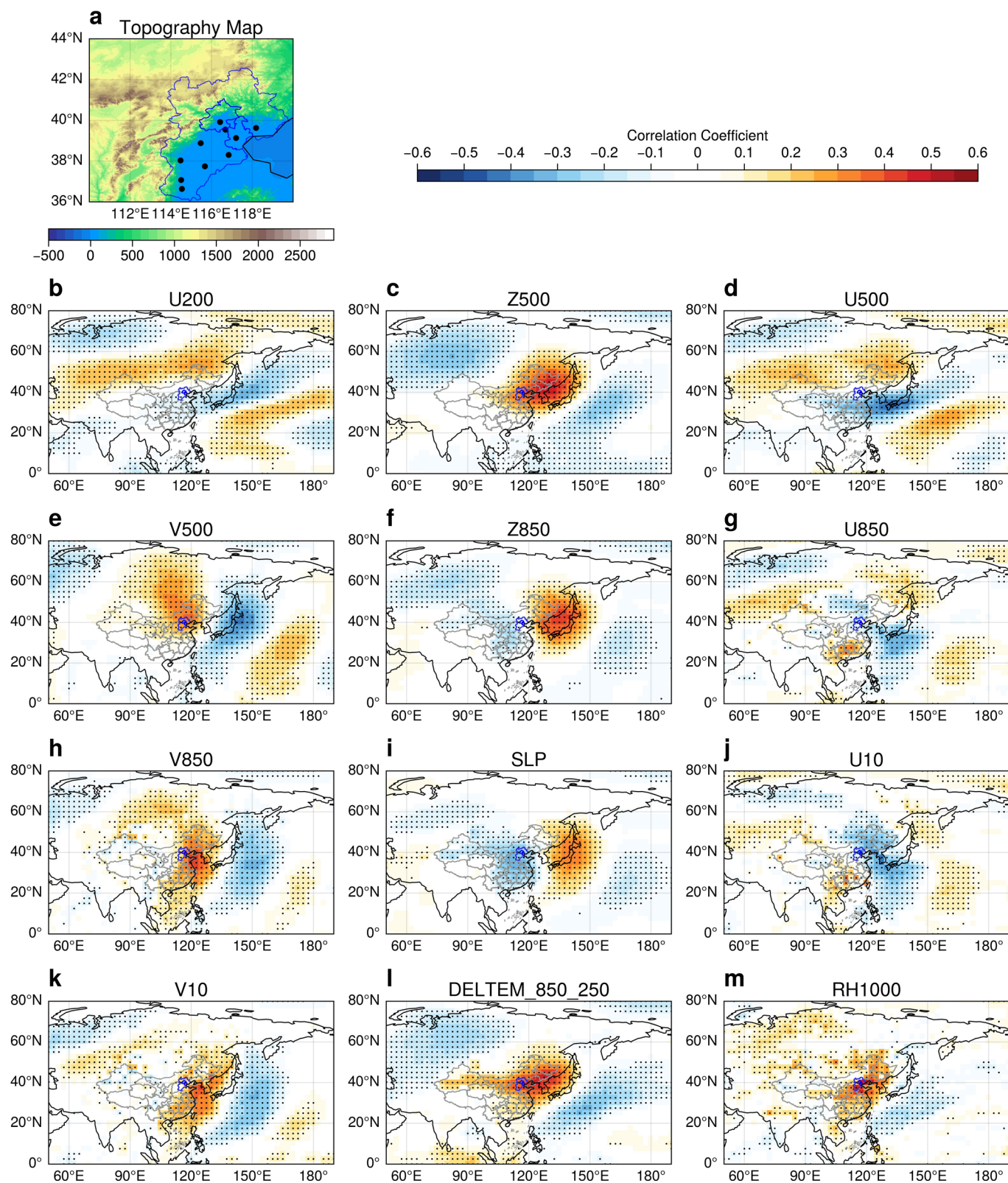
Extended data is available for this paper at <https://doi.org/10.1038/s41561-022-00933-2>.

Supplementary information The online version contains supplementary material available at <https://doi.org/10.1038/s41561-022-00933-2>.

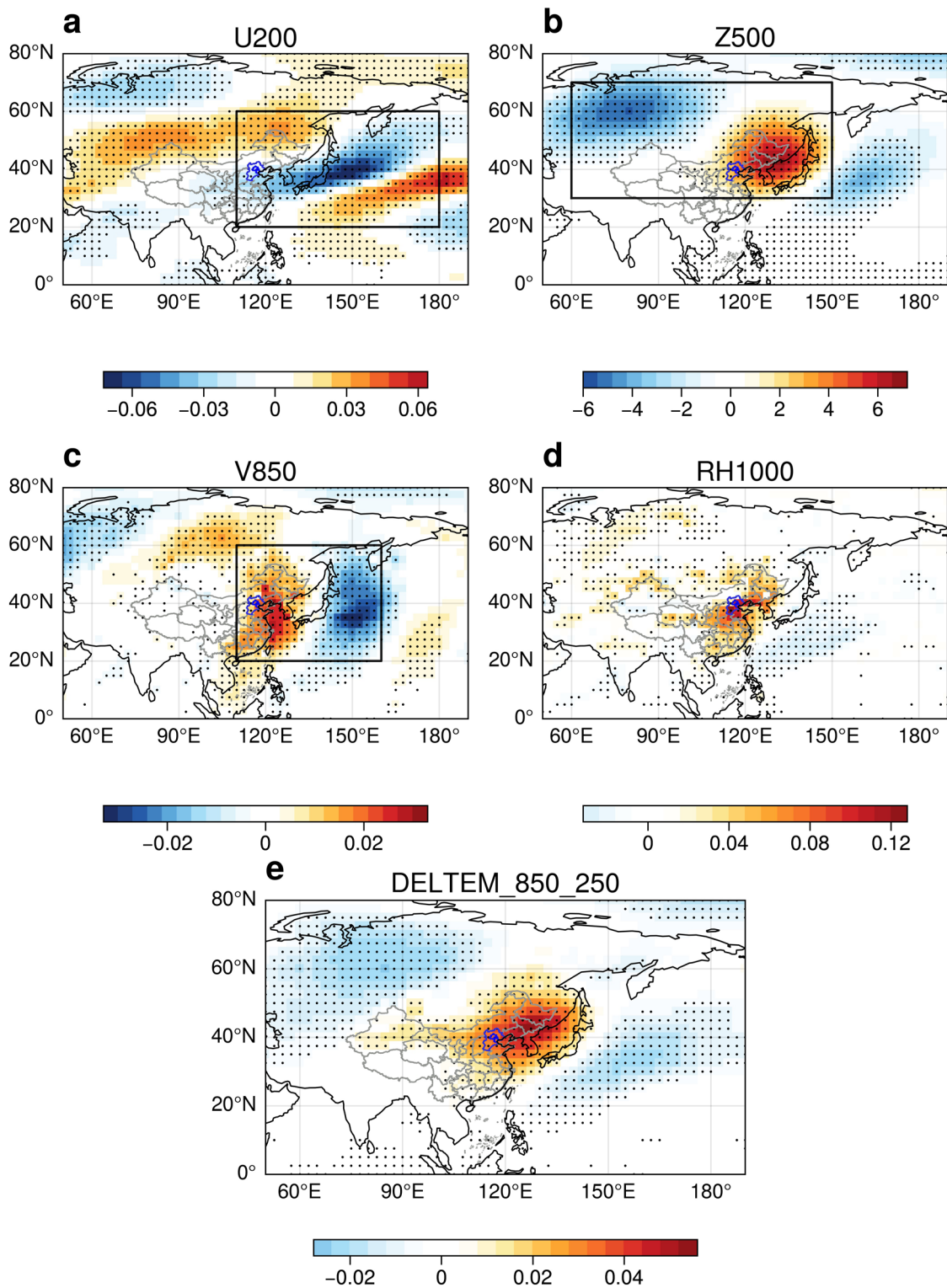
Correspondence and requests for materials should be addressed to Hong Liao.

Peer review information *Nature Geoscience* thanks the anonymous reviewers for their contribution to the peer review of this work. Primary Handling Editors: Xujia Jiang and James Super, in collaboration with the *Nature Geoscience* team.

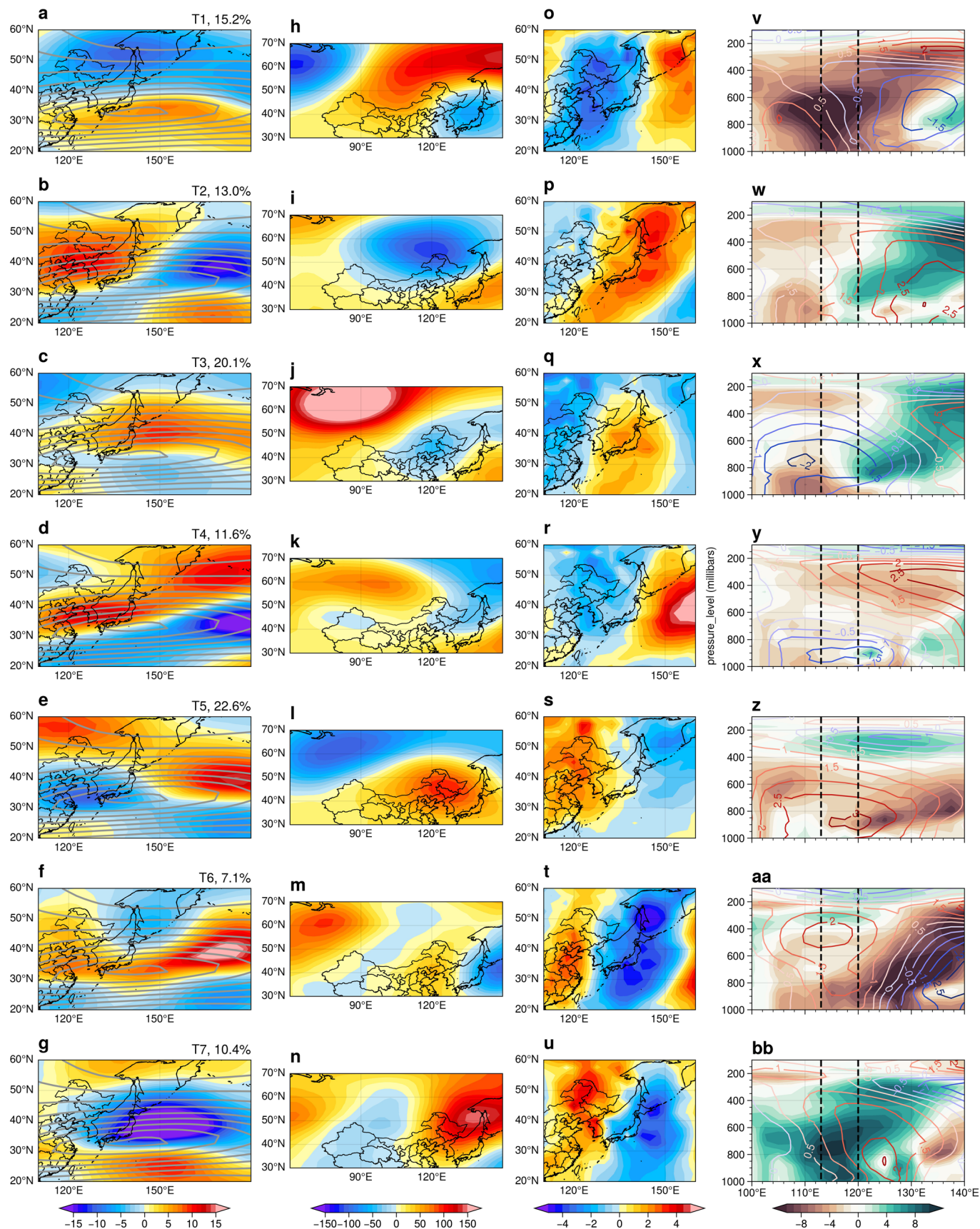
Reprints and permissions information is available at www.nature.com/reprints.



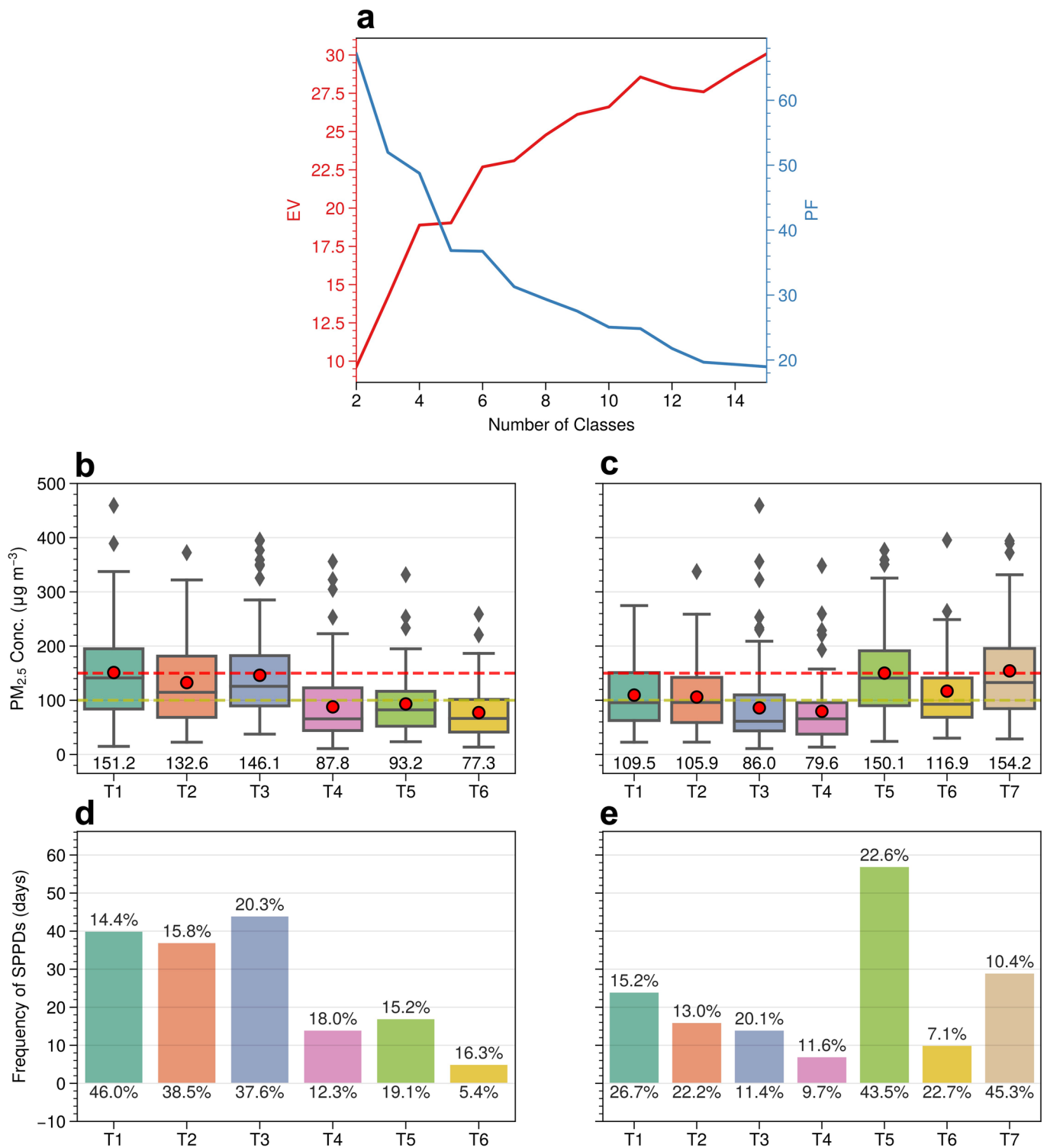
Extended Data Fig. 1 | Correlation between daily meteorology anomalies and winter $PM_{2.5}$. **a**, Topographic map of the North China Plain (shading, unit: m) and locations of cities (black dots) with observed $PM_{2.5}$ concentrations used in this study. **b–m**, Distribution of correlation coefficients between daily mean $PM_{2.5}$ concentrations and daily meteorological fields during DJFs from 2013 to 2019. Stippled regions in **b–m** denote those areas exceeding the 95% significance level based on the Student's *t*-test. The blue line is the boundary of the BTH region.



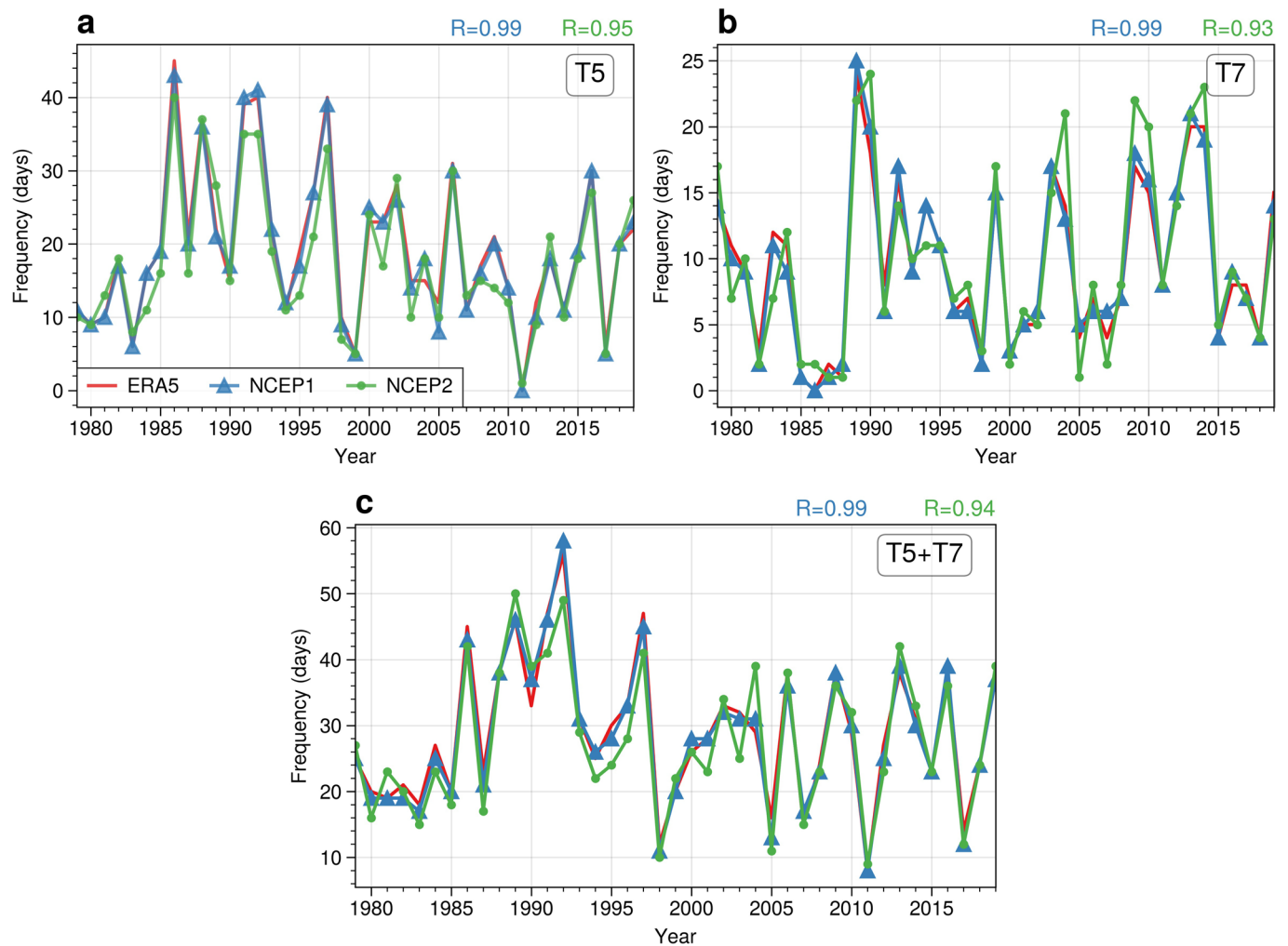
Extended Data Fig. 2 | Regression between daily meteorological anomalies and winter $PM_{2.5}$. Distribution of regression coefficients between daily mean $PM_{2.5}$ concentrations with daily (a) U200, (b) Z500, (c) V850, (d) RH1000 (relative humidity at 1000 hPa) and (e) Deltem_850_250 (vertical difference in the temperature anomalies between 850 hPa and 250 hPa) during DJFs from 2013 to 2019. Stippled regions denote those areas exceeding the 95% significance level based on the Student's t-test. The blue line is the boundary of the BTH region. The black rectangles in a-c are selected regions for each variable.



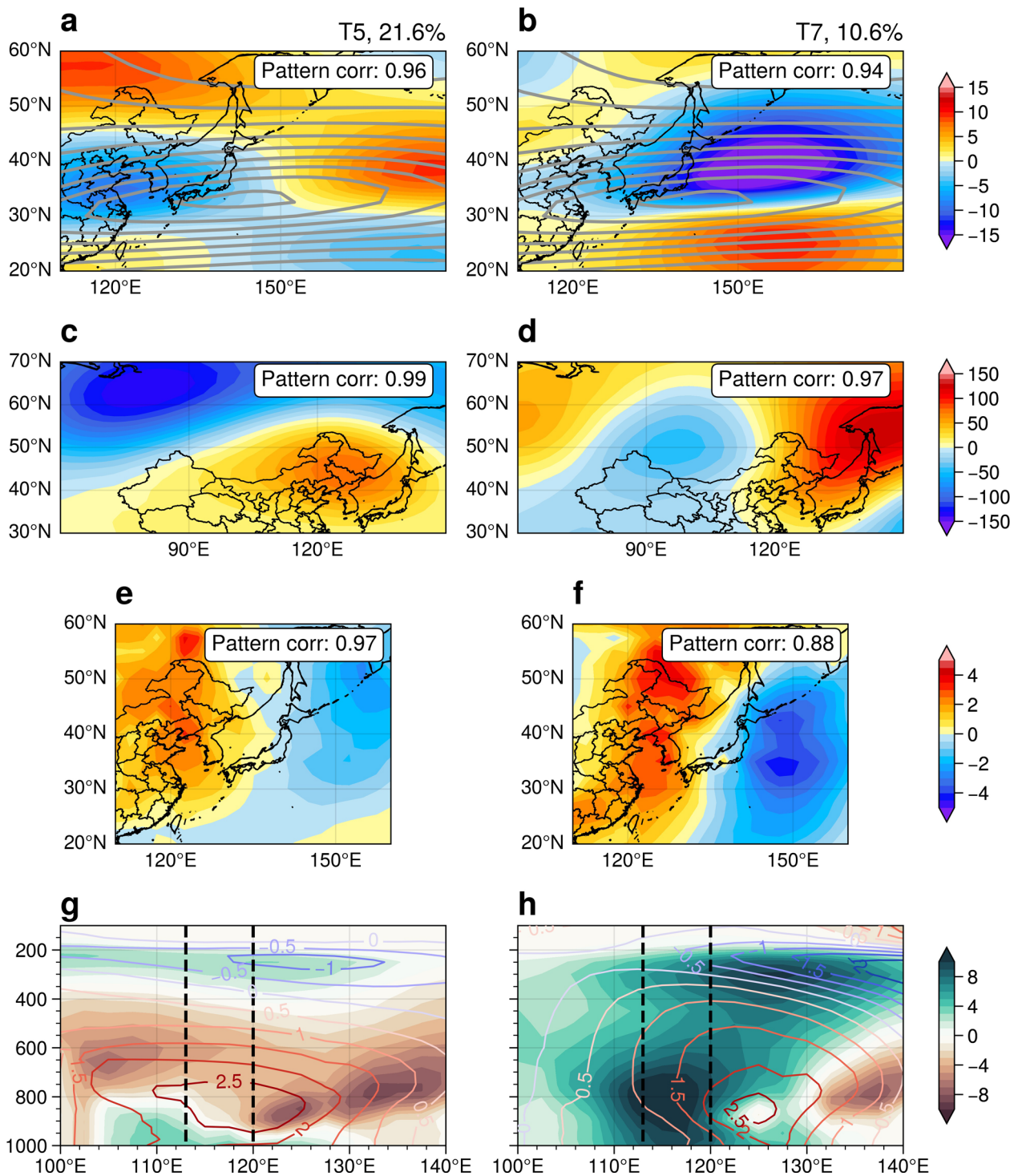
Extended Data Fig. 3 | Composited weather patterns for T1-T7 during the DJFs of 2013-2019. **a-g**, Composite anomalies of **(a-g)** U200 (units: $m\ s^{-1}$), **(h-n)** Z500 (units: m), **(o-u)** V850 (units: $m\ s^{-1}$), and **(v-bb)** pressure-longitude cross sections of the relative humidity (shadings, units: %) and temperature (contour, unit: $^{\circ}C$) for each weather type. The gray contours in **a-g** are the western jet streams calculated by the DJF means of U200 from 1979 to 2018. The cross sections in **v-bb** are averaged over 30-40°N, and areas between the two black dashed lines denote the BTH region.



Extended Data Fig. 4 | Evaluation for different classifications. **a**, The explained variation (EV) and pseudo-F (PF) values for different classifications. **b-e**, Box and whisker plots of the average $PM_{2.5}$ concentrations (**b, c**) and frequencies of SPPDs (**d, e**) under each Type for 6 (**b, d**) and 7 (**c, e**) classes in **a**. The red dots in boxes (**b, c**) denote mean $PM_{2.5}$ concentrations and their values are listed below boxes. The numbers above the histograms are the frequencies of each type in DJFs during 2013–2019, and those below the histograms are the SPPDs frequencies within each type.

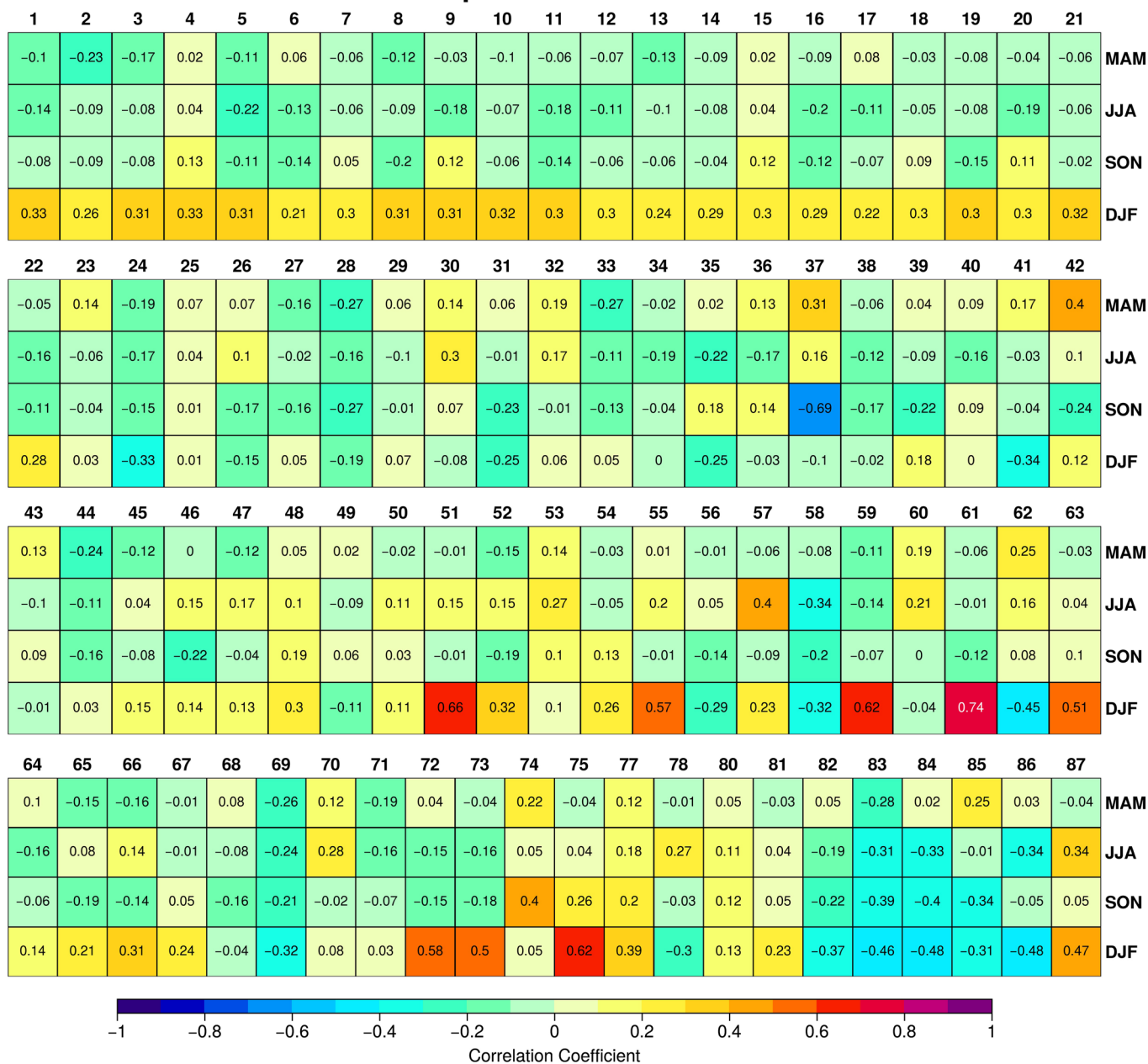


Extended Data Fig. 5 | Long-term variations of reconstructed conducive weather patterns using different reanalysis datasets. a–c, Time series of occurrence frequencies for the R-CWPs in winters of 1979–2019 by using the ERA5 (red), NCEP1 (blue), and NCEP2 (green) reanalysis datasets, respectively. The inset texts in the top right corner of each panel denote correlation coefficients between R-CWPs with ERA5 reanalysis and R-CWPs using NCEP1 and NCEP2 reanalysis in 1979–2019, respectively.



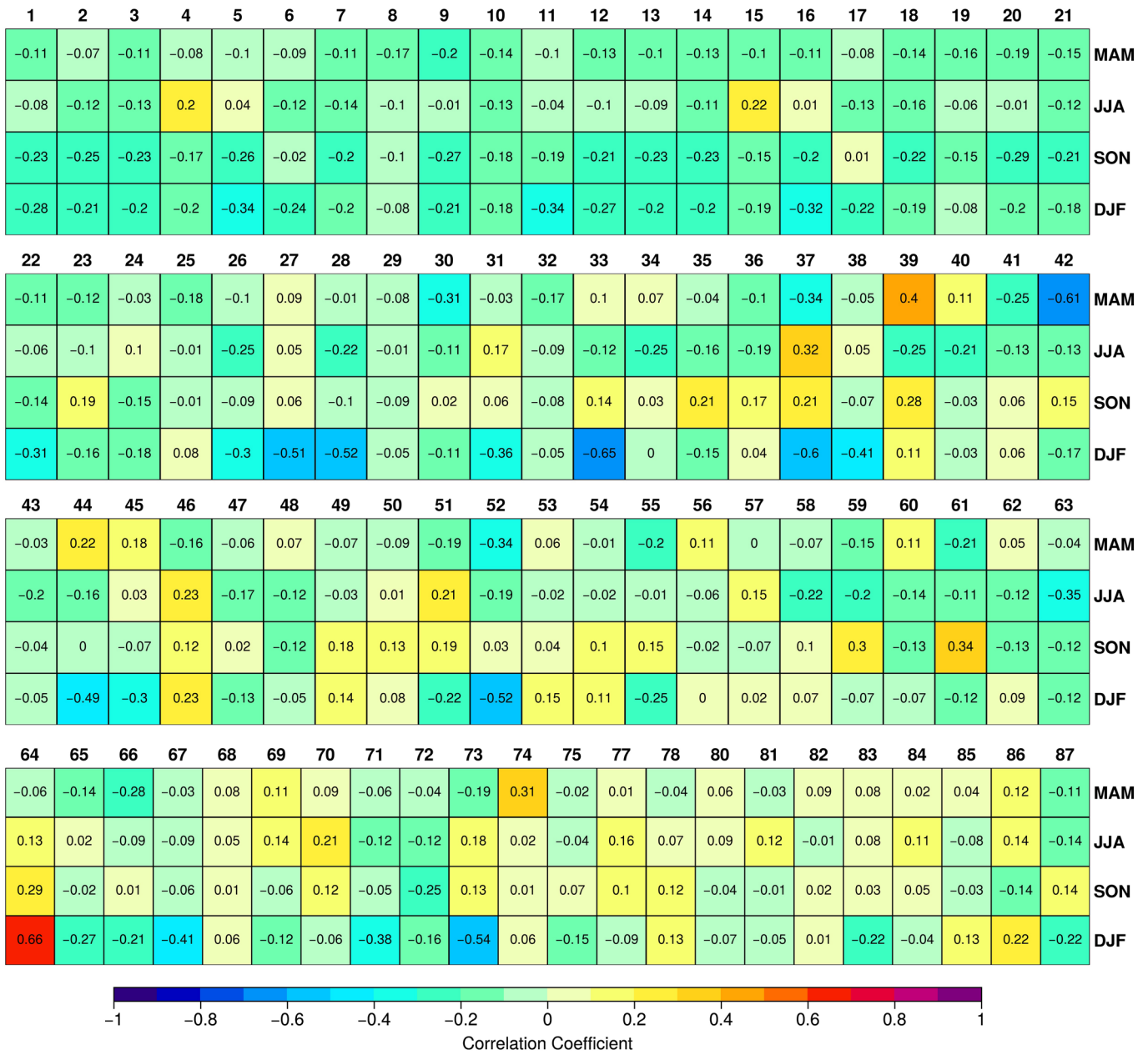
Extended Data Fig. 6 | Reconstructed conducive weather patterns for T5 and T7 over the years of 1979–2019. a–h. Composite anomaly distributions of (a, b) U200 (units: m s^{-1}), (c, d) Z500 (units: m), (e, f) V850 (units: m s^{-1}) and (g, h) pressure–longitude cross sections of the relative humidity (shadings, units: %) and temperature (contour, unit: $^{\circ}\text{C}$) for the reconstructed T5 and T7 weather types. The gray contours in a and b are the western jet streams calculated by the DJF means of U200 from 1979 to 2018. The cross sections are averaged over 30–40 $^{\circ}\text{N}$, and areas between the two black dashed lines denote the BTH region. The “Pattern corr” in a–f denote the pattern correlation between the composites in Fig. 1c–h and a–f.

Amospheric Indices & T5



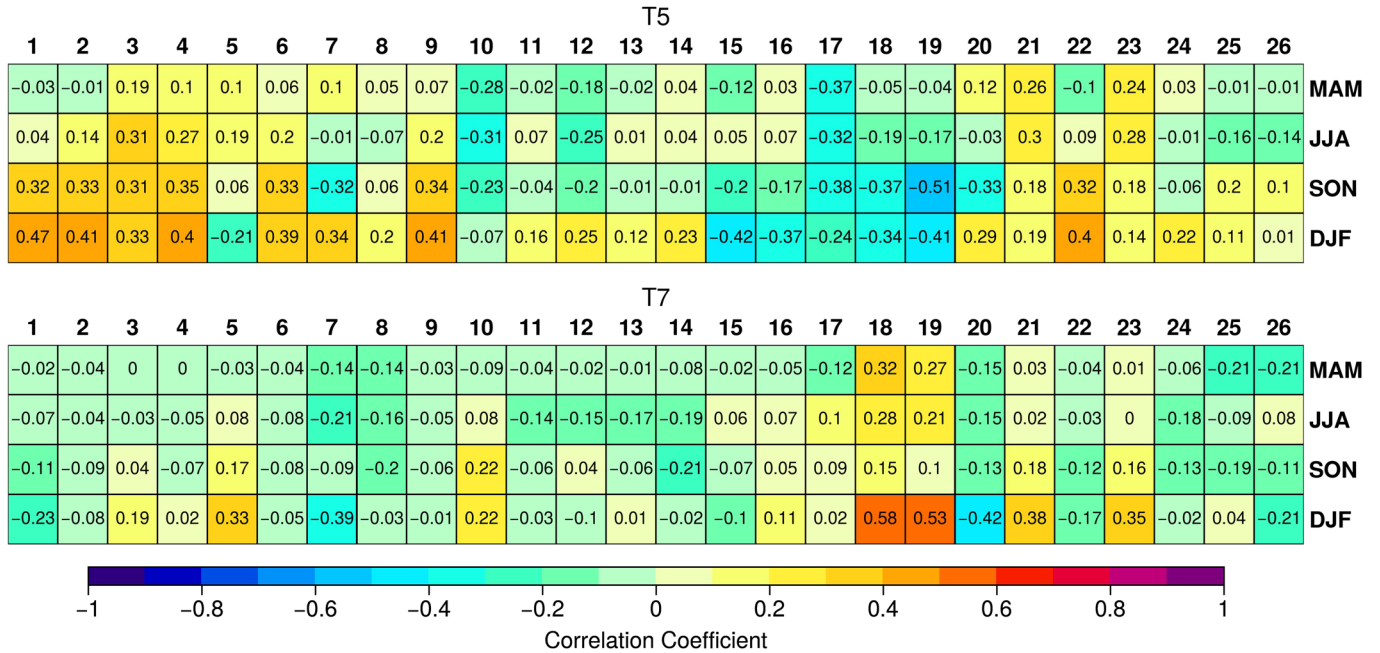
Extended Data Fig. 7 | Relationship between T5 and atmospheric indices. Heatmap of correlation coefficients between various atmospheric indices and frequency of reconstructed T5 weather pattern. Correlation coefficients between the time series of T5/T7 and climate indices in Extended Data Figs. 7-9 are all detrended to remove linear trends.

Amospheric Indices & T7



Extended Data Fig. 8 | Relationship between T7 and atmospheric indices. Heatmap of correlation coefficients between various atmospheric indices and frequency of reconstructed T5 weather pattern.

SST Indices



Extended Data Fig. 9 | Relationship between T5/T7 and SST indices. Heatmap of correlation coefficients between SST indices and frequency of reconstructed T5 (top panel) and T7 (bottom panel) weather pattern.